

*Journal of*  
***Mechanics of***  
***Materials and Structures***

**NUMERICAL AND EXPERIMENTAL STUDIES OF DEEP  
INDENTATION ON SINGLE CRYSTALS**

Yong X. Gan, Xi Chen and Manhong Zhao

***Volume 3, N° 8***

***October 2008***



mathematical sciences publishers

## NUMERICAL AND EXPERIMENTAL STUDIES OF DEEP INDENTATION ON SINGLE CRYSTALS

YONG X. GAN, XI CHEN AND MANHONG ZHAO

Indentation tests with large penetration depths have been used to study the plastic deformation behavior of materials. In this work, finite element simulations of wedge indentation into face-centered cubic single crystals were performed. Numerical solutions to the stresses and shear strains within the single crystals indented with a relatively large penetration depth were obtained. The crystal lattice rotation map of the indented crystals was also shown. Indentation experiments were conducted on copper crystals and the results were used to validate the numerical predictions. Comparison of the numerical solutions to the crystal lattice rotation with the experimentally measured lattice rotation map was made. The main features of the crystal lattice in-plane rotation map from the finite element simulations are also found on the map developed from the electron backscatter diffraction measurements. Both simulations and experimental measurements reveal the same dislocation structures as evidenced by the slip sectors underneath the wedge indentation zone.

### 1. Introduction

Indentation is useful for obtaining load-displacement data and the data may be used for mechanical property evaluation [Beghini et al. 2006], post-yielding analysis [Habbab et al. 2006], and materials rheology study [Bigot et al. 2005]. Vlassak and Nix [1994] measured the elastic properties of anisotropic materials such as copper and brass under indentation. The indentation size effect was studied to reveal the variation of measured properties with the applied loading levels. Based on the indentation studies on titanium and aluminum, it is found that the contact surface area between the specimens and the indenter causes the variation of microhardness [Iost and Bigot 1996]. In the work performed by Gerberich et al. [2002], the indentation size effect is correlated to the ratio of the energy of newly created surface and the plastic strain energy dissipation. The ratio of contact surface area to plastic volume remains constant if the indentation depth is within several hundred nanometers. Another phenomena related to shallow indentation, the surface step effect, was found [Zimmerman et al. 2001], meaning that the load needed to nucleate dislocations decreases significantly when indenting close to a surface step.

From indentation tests, important information about dislocation activities within materials can be obtained. For example, Kysar et al. [2007] used indentation data to calculate the geometrically necessary dislocation density. The condition for dislocation pile-up under a conical nanoindenter is determined by Zaafarani et al. [2008]. Bhattacharya and Nix [1991] showed how to determine the shapes of plastic zones under indenters. They also clarified the effects of shear modulus, bulk modulus and indenter angle on the hardness of hard and soft materials. Laursen and Simo [1992] provided an approach to

---

*Keywords:* finite element simulation, indentation, plastic deformation, copper crystal, stress field, shear strain, electron backscatter diffraction, crystal lattice rotation, slip, dislocation structure.

computing the hardness, contact stiffness, effective composite modulus, and surface profile under load and thus the amount of pileup (or sink-in) around the indenter in the fully loaded configuration, as well as the variation of the actual contact area during indenter withdrawal, can be predicted. Marx and Balke [1997] identified the influence of material properties on the unloading response. Bolshakov and Pharr [1998] showed how to use indentation load-displacement data to identify when pileup occurs. The work performed by Giannakopoulos et al. [1994] evaluated the hardness formulae for materials under Vickers indentation tests.

Studies of spherical indentation into a half-space have been performed for a long time, as shown in the works performed by Follansbee and Sinclair [1984], Sinclair et al. [1985], and Hill et al. [1989], which provide important information about hardness, contact pressure distributions, and the transition from the initial elastic regime to the fully plastic contact regime. Cylindrical indentation induced deformation in face-centered cubic (FCC) metal single crystals was examined in our earlier work [Gan et al. 2007]. For sharp indentation tests using conical, pyramidal, or wedge indenters, the behavior of tested materials may not be deduced directly. So, numerical simulations were used [Pelletier 2006] to predict the deformation of the indented region. For example, Qu et al. [2006] used finite elements (FE) to simulate the mechanism-based strain gradient plasticity in an indented iridium specimen. Indentation with small or moderate penetration depth has been studied for evaluating the elastic-plastic properties of materials such as thin films [Zhao et al. 2006; 2007]. Deep penetrating indentation tests may be used to study the plastic deformation behavior of materials. At the micron length scale, materials often exhibit heterogeneous behavior as shown by Rashid et al. [1992] via the slip of copper single crystals at different loading rates. Havner and Yu [2005] analyzed the finite double slip behavior in FCC crystals. The number and orientation of active slip systems are dependent and may vary during an indentation test [Bouvier and Needleman 2006]. Constitutive modeling of materials at different finite deformation states was performed [Naghdabadi et al. 2005]. A deformation gradient based kinematic hardening model was reported [Wallin and Ristinmaa 2005]. Lattice orientation effects on plastic deformation and damage evolution in FCC single crystals were also studied [Potirniche et al. 2006].

The work on simulations of indentation into single crystals spans atomic discrete simulations [Miller et al. 2004], nanoscale plasticity simulations [Horstemeyer et al. 2001], mesoscale investigation [Yoshino et al. 2001], micromechanics based FE analysis [Premachandran and Horii 1994], and quasicontinuum analysis [Tadmor et al. 1996]. For example, the simulation at atomic scale levels using molecular dynamics methodologies was presented by Miller et al. [2004]. Atomistic simulations of elastic deformation and dislocation nucleation during nanoindentation were performed by Lilleodden et al. [2003]. Horstemeyer et al. [2001] investigated the structure-property relations for plasticity at different length scales through simulations using embedded atom potentials. Three dimensional finite element simulations of dislocation nucleation under indentation were investigated based on the analysis of nanoscale contact of single crystal copper by a cylindrical indenter [Zhu et al. 2004], and by a conical indenter [Wang et al. 2004]. Based on three dimensional FE analysis, the complex equilibrium crack front of indentation into thin film coated on a thick silicon crystal substrate was identified [Xia et al. 2004], and the indent-induced plastic zone in FCC crystals was defined [Fivel et al. 1998]. Simulation of the strain gradient effects on a microscopic strain field was also performed [Shu and Barlow 2000]. Quasicontinuum analysis [Tadmor et al. 1996] allows us to obtain simultaneous solutions for continuum and atomistic length scales. However, the computation (either atomistic or multiscale) is very expensive and not applicable to

large length scales. It cannot simulate very deep indents. Therefore, FE simulations of indentation into single crystals were used to predict the plastic properties of single crystals, for example, Al, Ni, and Pb [Xu and Rowcliffe 2002], and MgO [Yoshioka 1991; Xu and Rowcliffe 2002]. However, there is very little work on validating the numerical solutions using experimental results.

In this work, we simulated the wedge indentation in copper single crystals with special orientations. Comparison of the finite element solutions with experimental results was made. The paper is organized as follows. First, the numerical simulations based on finite deformation theory of single crystal plasticity will be presented. Implementation of finite element simulations will be delineated. Second, indentation test procedures will be given and the lattice rotation measurement will be briefly described. Then, stress, shear strain, and in-plane lattice rotation solutions from the FE simulations will be given. Subsequently, the indentation experimental results will be presented. Following that, comparison of the numerical solutions and the experimentally measured lattice rotation results will be carried out to validate the finite element solutions. The novelty of this work is in testing the numerical predictions through experimental results.

## 2. Finite element simulation

The finite element analysis was performed using the commercial software ABAQUS. A user-material subroutine for single crystal plasticity was used in implementation of the simulations for copper single crystals. The subroutine is based on the framework of kinematical theory for the mechanics of single crystals [Turkmen et al. 2004]. For the finite deformation of single crystals,

$$\hat{\mathbf{D}} + \hat{\mathbf{\Omega}} = \hat{\mathbf{F}}\hat{\mathbf{F}}^{-1}, \quad \mathbf{D}^{\mathbf{P}} + \mathbf{\Omega}^{\mathbf{P}} = \sum_{k=1}^n \dot{\gamma}^{(k)} \hat{\mathbf{s}}^{(k)} \otimes \hat{\mathbf{m}}^{(k)},$$

where  $\mathbf{F}$  is the deformation gradient,  $\mathbf{D}$  stands for the symmetric stretching tensor and  $\mathbf{\Omega}$  is the spin tensor, which can be decomposed into elastic parts ( $\hat{\cdot}$ ) and plastic parts ( $\cdot^{\mathbf{P}}$ ). The superscript  $k$  denotes the  $k$ -th slip system,  $\dot{\gamma}^{(k)}$  is the shear strain rate,  $n$  is the total number of the active slip systems,  $\hat{\mathbf{s}}^{(k)}$  and  $\hat{\mathbf{m}}^{(k)}$  are unit vectors along the slip direction and normal to the slip plane in the reference configuration, respectively.

The constitutive relation for single crystals under finite deformation is  $\hat{\hat{\sigma}} + \sigma(I : \hat{\mathbf{D}}) = \mathbf{L} : \hat{\mathbf{D}}$ , where  $L$  is the tensor of elastic moduli and  $\hat{\hat{\sigma}}$  is the corotational stress rate on axes that rotate with the crystal lattice.  $\hat{\hat{\sigma}}$  can be expressed as  $\hat{\hat{\sigma}} = \tilde{\sigma} + (\mathbf{\Omega} - \hat{\mathbf{\Omega}})\sigma - \sigma(\mathbf{\Omega} - \hat{\mathbf{\Omega}})$ , where  $\tilde{\sigma}$  is the corotational stress rate on axes rotating with the material, which is  $\tilde{\sigma} = \dot{\sigma} - \mathbf{\Omega}\sigma + \sigma\mathbf{\Omega}$ . The Schmid stress and the rate of Schmid stress are given as

$$\tau^{(k)} = \hat{\mathbf{m}}^{(k)} \frac{\rho_0}{\rho} \sigma \hat{\mathbf{s}}^{(k)}, \quad \dot{\tau}^{(k)} = \hat{\mathbf{m}}^{(k)} \left[ \hat{\hat{\sigma}} + \sigma(I : \hat{\mathbf{D}}) + \sigma \hat{\mathbf{D}} - \hat{\mathbf{D}}\sigma \right] \hat{\mathbf{s}}^{(k)},$$

where  $\rho_0$  and  $\rho$  are the mass density in the reference and current states, respectively.  $\tau^{(k)}$  is the resolved shear stress onto the  $k$ -th slip system.

To find  $\dot{\gamma}^{(k)}$  we used a rate-dependent relation for single crystals as proposed by Hutchinson [1976]:

$$\dot{\gamma}^{(k)} = \dot{\gamma}_0 \operatorname{sgn}[\tau^{(k)}] \left| \frac{\tau^{(k)}}{g^{(k)}} \right|^m,$$

where  $\dot{\gamma}_0$  is the reference strain rate,  $\tau^{(k)}$  is the applied resolved shear stress,  $m$  is the rate sensitivity exponent, and  $g^{(k)}$  is related to the critical resolved shear stress of the  $k$ -th slip system.

The evolution of strength is related to the strain rate,  $\dot{\gamma}$ , and the slip hardening moduli  $h_{kl}$  by

$$\dot{g}^{(k)} = \sum_{l=1}^n h_{kl} \dot{\gamma}^{(l)}.$$

The hardening moduli are found in different forms depending on the model used [Kysar 2001]. In the Bassani–Wu hardening model,  $h_{kl}$  takes the form

$$h_{kk} = \left\{ (h_0 - h_\infty) \cosh^{-2} \left[ \left| \frac{(h_0 - h_\infty) \gamma^{(k)}}{\tau_\infty - \tau_0} \right| + h_\infty \right] + h_\infty \right\} G(\gamma^{(l)}),$$

$$h_{kl} = q h_{kk}, \quad (k \neq l)$$

where  $h_0$  is the initial value of hardening modulus, and  $h_\infty$  is the saturated value of hardening modulus.  $\tau_0$  is the initial value of  $g^{(k)}$ .  $\tau_\infty$  is the stress at which hardening moduli reach  $h_\infty$ .  $G$  is a function related to cross-hardening that occurs between slip systems.

In order to formulate the finite element program, the increment of shear strain is formulated as

$$\Delta \gamma^{(k)} - (1 - \Theta) \Delta t \dot{\gamma}^{(k)} - \Theta \Delta t \dot{\gamma}^{(k)} f^{(k)} \frac{\tau_t^{(k)} + \Delta \tau_t^{(k)}}{g_t^{(k)} + \Delta g^{(k)}} = 0,$$

where  $\Theta$  is the interpolation parameter which takes a value between 0 and 1,  $f^{(k)}$  is a dimensionless function which reveals the dependence of strain rate on the stress, and  $\Delta \tau^{(k)}$  and  $\Delta g^{(k)}$  are the increments of resolved shear stress and current strength in the  $k$ -th slip system within the time increment  $\Delta t$ , respectively.

The increments of resolved shear stress,  $\Delta \tau^{(k)}$ , depend on the strain increments  $\Delta \epsilon_{ij}$  and the stress as

$$\Delta \tau^{(k)} = \left[ \tilde{E}_{ijab} \mu_{ab}^{(k)} + \omega_{ia}^{(k)} \sigma_{ja} + \omega_{ja}^{(k)} \sigma_{ia} \right] \left[ \Delta \epsilon_{ij} - \sum_{k=1}^n \mu_{ij}^{(k)} \Delta \gamma^{(k)} \right],$$

where  $\tilde{E}_{ijab}$  are the elastic moduli.  $\mu_{ij}^{(k)}$  is the Schmid factor, and  $\omega_{ij}^{(k)}$  is a tensor related to the spin tensor  $\Omega$  and  $\hat{\Omega}$ , which are

$$\mu_{ij}^{(k)} = \frac{1}{2} [\hat{s}_i^{(k)} \hat{m}_j^{(k)} + \hat{s}_j^{(k)} \hat{m}_i^{(k)}], \quad \omega_{ij}^{(k)} = \frac{1}{2} [\hat{s}_i^{(k)} \hat{m}_j^{(k)} - \hat{s}_j^{(k)} \hat{m}_i^{(k)}], \quad \Omega_{ij}^{(k)} - \hat{\Omega}_{ij}^{(k)} = \sum_{k=1}^n \omega_{ij}^{(k)} \dot{\gamma}^{(k)}.$$

Therefore, for given strain increments, the increments of shear strain can be determined. Then, the stress increments,  $\Delta \sigma_{ij}$ , can also be solved by

$$\Delta \sigma_{ij} = \tilde{E}_{ijab} \Delta \epsilon_{ab} - \sigma_{ij} \Delta \epsilon_{aa} - \sum_{k=1}^n \left[ \tilde{E}_{ijab} \mu_{ab}^{(k)} + \omega_{ia}^{(k)} \sigma_{ja} + \omega_{ja}^{(k)} \sigma_{ia} \right] \Delta \gamma^{(k)}.$$

In addition, the explicit forms of the increments of lattice rotation are found to be [Asaro 1983]

$$\Delta \hat{s}_i^{(k)} = \left\{ \Delta \epsilon_{ij} + \Omega_{ij} \Delta t - \sum_{k=1}^n [\mu_{ij}^{(k)} + \omega_{ij}^{(k)}] \Delta \gamma^{(k)} \right\} \hat{s}_j^{(k)},$$

$$\Delta \hat{m}_i^{(k)} = - \left\{ \Delta \epsilon_{ji} + \Omega_{ji} \Delta t - \sum_{k=1}^n [\mu_{ji}^{(k)} + \omega_{ji}^{(k)}] \Delta \gamma^{(k)} \right\} \hat{m}_j^{(k)}.$$

The convergence of the finite element simulations is assured by choosing a relatively small time incremental step size in the users' subroutines.

In this work, the numerical computation generates errors on the order of  $\Delta t^2$ , where  $\Delta t$  is the step size used in simulation. The indentation contact, loading, and unloading were set under displacement control to achieve better convergence properties than in the case of under load control. The critical shear stress,  $\tau$ , for the copper single crystals was assumed to be 61 MPa. This is based on the experimental results. We did compression tests (along the [001] direction) on three copper crystal samples with the dimensions  $5 \times 5 \times 10$  mm to find the yield point. The average load at the yield point was used to calculate the shear strength by multiplying the Schmid factor related to this crystallographic orientation. The element used in the simulation is a plane strain reduced integration, hybrid element (CPE4RH). The mesh is schematically shown in Figure 1. The crystal in a quadrant and the  $90^\circ$  wedge indenter are put together in the drawing. Figure 1a is the global view of the indenter and the half single crystal with the mesh. Figure 1b shows the finer mesh close to the tip of the indenter. There are three mesh sizes. The first 12,880 elements in the region closed to the indenter tip have the mesh size  $1.5 \times .5 \mu\text{m}$ . The 16,100 elements away from the indenter tip have the mesh size of  $3 \times 1.5 \mu\text{m}$ . The rest of 19,320 elements far away from the indenter have varied mesh sizes. The mesh size changes from  $1.5 \times 3 \mu\text{m}$  to  $4 \times 3 \mu\text{m}$ . It must be pointed out that some variables may be chosen dimensionless in the simulations. For example, the mesh and indentation depth could be set as dimensionless by normalizing these parameters by the indenter size. However, since the indenter is assumed as analytically rigid, the yield strength of the indenter in this case approaches

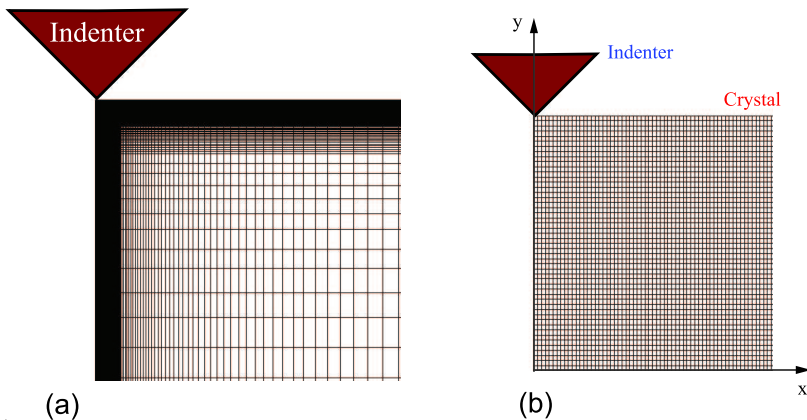


**Figure 1.** Mesh for the finite element simulation of wedge indentation: (a) global view of the mesh and the wedge indenter and (b) mesh close to the wedge indenter tip and the boundaries of the crystal, the dark region in (a).

infinity. This might cause convergence problems if we would normalize the yield strength of the crystal specimen by the yield strength of the indenter. The shear strength of copper crystal, 61 MPa, is used in the simulation. This unit is equivalent to  $\mu\text{N}/\text{mm}^2$ . Consequently, the mesh size of the crystal and the indenter penetration depth are also carrying the unit of  $\mu\text{m}$ . Numerical tests of mesh convergence were carried out to ensure that the presented results were independent of further mesh refinement. Excessive mesh distortion was not observed during simulation and thus remeshing was not used.

The wedge indenter is defined as analytically rigid and the contact between the indenter and the crystal is frictionless. In the finite element analysis, lattice rotation and stresses were solved incrementally by ABAQUS. The constitutive properties are chosen as elastic-ideally plastic because the load increases almost linearly with the indentation penetration depth as will be shown in Figure 7b. From this behavior and taking into account that the indentation contact area is increasing linearly, we concluded that the nominal strength of the copper single keeps almost the same. Therefore the material is very close to an elastic-ideally plastic state under the indentation conditions. The power-law rate-dependent relationship proposed by Hutchinson [1976] and delineated by Connolly and McHugh [1999], Peirce et al. [1983], and Savage et al. [2004], was applied in the simulation. Since elastic-ideally plastic properties are used in this simulation, the function related to critical resolved shear stress of the  $k$ -th slip system is taken as a constant. The reference strain rate was  $10^{-3} \text{ s}^{-1}$ , and the rate sensitivity exponent was 50.0. The stress at which hardening moduli are saturated was 109.5 MPa. The ratio of latent over self hardening moduli of various sets of slip systems was 1. During the simulation, the minimum iteration step used was  $1 \times 10^{-9}$  and the maximum step was  $5 \times 10^{-5}$  and 20000 increments were performed in the loading and unloading simulations. The computation was implemented on a computer with CPU frequency of 2.88 GHz and the CPU time of 43200 s.

### 3. Experimental methods

Wedge indentation tests were performed on copper single crystal specimens. Three specimens were used in the tests. All the results were based on the average of the data obtained from the three specimens. The wedge indenter used in this study had an apex angle of  $90^\circ$ . The indenter was made of tungsten carbide bonded by a ferrous alloy. The indentation direction is along the  $[00\bar{1}]$  crystallographic orientation of the copper single crystals. During indentation tests, the load and displacement data were recorded. After the indentation, the midsection of the single crystal specimens with plane strain deformation conditions was exposed through cutting. This exposed plane corresponds to the crystallographic plane of (110). After being cut, the copper single crystal specimens were put into a compacted fixture and the indented surface was filled with a polymer to protect the indented surface from mechanical damage during subsequent processes.

The surfaces of the crystals were mechanically polished following the procedures as follows. Sandpaper (grit 600) was used to grind the surface under minimum pressure along one direction until any deep scratches from the previous cutting process were invisible. Water was used as lubricant and coolant for preventing the polishing surface from becoming overheated. The purpose of this polishing procedure is to remove the possible deep deformation layer from the previous grinding processes. The grinding/polishing along one direction can prevent rounded corner formation along the edges of the polished surface. The polish direction was changed by  $90^\circ$  to the same grit 600 sand paper, with even less pressure applied

until the scratches from the previous polishing procedure were invisible. Water was applied continuously. The purpose of this polishing procedure is to remove the possible residual stress layer generated from previous polishing. The specimen was washed with tap water to prevent any coarse abrasive going into the next polishing procedure. The procedure was repeated using 1200 grit sandpaper. Fine polishing was performed using diamond compound with diameter of  $6\ \mu\text{m}$ . The specimens were then washed in soapy water. Having been polished mechanically, the copper single crystals were cleaned. The cleaned copper crystals were surface activated in a 10% HCl solution followed by rinsing in deionized water. After that, the surface of (110) of the single copper crystals were electrochemically polished in an 85% orthophosphoric acidic solution.

Scanning electron microscopic (SEM) examination and electron backscatter diffraction (EBSD) data acquisition were carried out on a scanning electron microscope. Figure 2a is an SEM image showing the indented single crystal. For EBSD measurement, a polycrystalline copper block was put on the right-hand side of the copper single crystal specimen for subtracting background signals, and a piece of silicon single crystal with the surface normal of [001] orientation was aligned on the left-hand side of the copper single crystal at the same level with the same tilt angle of  $70^\circ$ . The Si single crystal was used for detector orientation calibration and for projection parameter calibration. Figure 2b schematically shows the relative positions of the polycrystal, the single crystal Cu specimen, and the Si single crystal. The EBSD measurement was carried out on the middle section of the specimen at a tilt angle of  $70^\circ$ . Following the calibration, surface mapping was performed at an acceleration voltage of 20 kV. The EBSD mapping data were saved for subsequent analysis.

#### 4. Results and discussion

In this section, both simulation and experimental results of wedge indentation into copper single crystals will be presented. The finite element simulation results, including the stress solutions, shear strain solutions, and lattice rotation map, will be given first. Then, the experimental data will be given. The finite element solutions will be compared with the experimental results.

**4.1. Finite element solutions.** The finite element simulation results will be presented in the following three parts. First, numerical solutions for stresses will be shown. Second, the numerical solutions to

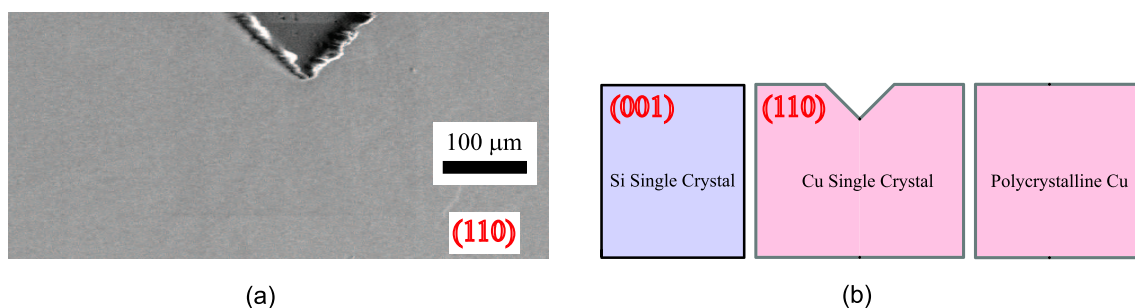


**Figure 2.** SEM image of the indented specimen and configuration for EBSD measurement: (a) SEM image of the indented specimen and (b) specimen alignment for the EBSD data acquisition.

shear strains associated with the slip of different slip systems will be shown. Then, the solution for the in-plane crystal lattice rotation will be given.

The finite element solutions for the normalized in-plane stress components of  $\sigma_{11}/\tau$ ,  $\sigma_{12}/\tau$ , and  $\sigma_{22}/\tau$  for the wedge indented copper crystal are shown in Figure 3a–c. From the results shown in both Figure 3a and c, we can see that underneath the indenter tip, the region within the copper single crystal was severely compressed because both  $\sigma_{11}/\tau$  and  $\sigma_{22}/\tau$  are negative. Farther away from the indentation tip, the region shows position value of  $\sigma_{11}/\tau$  and  $\sigma_{22}/\tau$ . The shear stress  $\sigma_{12}/\tau$ , as shown in Figure 3b, reveals a highly heterogenous and anisotropic behavior related to the indentation. The rapid change in shear stress is found in the areas both underneath the indenter tip and far below the indenter/single crystal contact region.

In order to define the shear strain on each activated slip system, a schematic drawing to show the physical orientations of all the most favorable slip systems associated with the special crystallographic orientation of the copper crystal under indentation is given in Figure 4. The numerical results of plastic shear strain on these slip systems,  $\gamma^{(n)}$ , were obtained.  $n$  is an integer with the values of 1, 2, and 3. The results of shear strains for different slip systems are output as solution dependent variables (SDVs).

Figure 5 shows the solutions for the plastic strain in the copper single crystal associated with the wedge indentation. Figure 5a–c illustrate the shear strain from each individual slip system as sketched in Figure 4. The plastic strain from all the three slip systems is given in Figure 5d. It is noted that  $\gamma^{(1)}$  refers to the shear strain due to the dislocation motion of slip system (1),  $\gamma^{(2)}$  stands for the shear strain due to the dislocation motion of slip system (2),  $\gamma^{(3)}$  is the shear strain due to the dislocation motion of slip

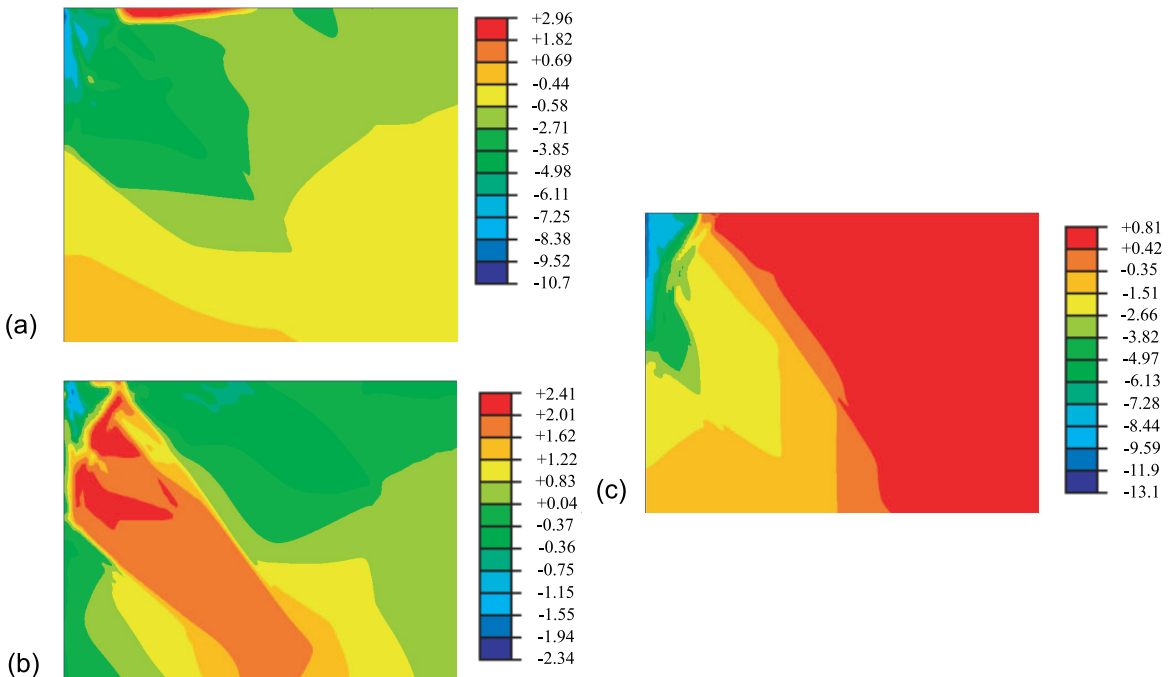


**Figure 3.** Numerical solutions to the stress components: (a)  $\sigma_{11}/\tau$ , (b)  $\sigma_{12}/\tau$ , and (c)  $\sigma_{22}/\tau$ .

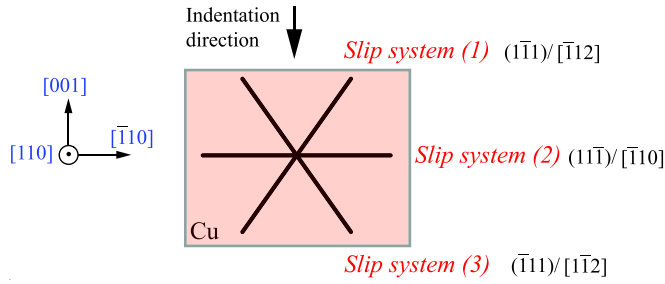
system (3), and  $\gamma$  refers to the total shear strain due to the dislocation motion of all the three slip systems. It can be seen from Figure 5a that  $\gamma^{(1)}$ , the shear strain due to the dislocation motion of slip system (1), takes significantly higher values on the right side of the indented region. However, the  $\gamma^{(2)}$  and  $\gamma^{(3)}$  as shown in Figure 5b and c, respectively, are considerably low in this region, where  $\gamma^{(2)}$  represents the shear strain from slip system (2) and  $\gamma^{(3)}$  stands for the shear strain from slip system (3). Thus, the numerical simulation predicts that the primary slip system in this region is slip system (1). As will be shown in Section 4.2, the EBSD experimental data about the in-plane lattice rotation define different regions where the dislocation motion of each of the three slip systems dominates the plastic deformation in a specific slip sector. For example, in the right hand side region adjacent to the extension line of the indenter tip, the dislocation motion is mainly due to the activation of slip system (1). Therefore, it is shown that the numerical predictions compare well with the experimental results. The results shown in Figure 5a–c also provide the information about the size of the plastic zone. It is found that the plastic zone is not just limited to the region underneath the indenter tip. Rather, it propagates into the crystal at least twice as far as the indentation penetration depth.

Figure 6 is the in-plane crystal lattice rotation map obtained from the finite element simulation. The unit of the lattice rotation angle is degree, which is calculated from the specific SDVs in the ABAQUS finite element simulation program. Comparison with the experimental results shown in Section 4.2.2 will be made later. The unit of lattice rotation as shown in Figure 6 is degree. The main features of the in-plane rotation from the simulation are as follows: In the lower left part of Figure 6, a region with negative lattice rotation can be found. This is due to the active dislocation movement of slip system (1). The existence of such a negative lattice rotation region can be validated by the experimental results as will be illustrated in Section 4.2.

The righthand side region adjacent to the lattice negative rotation region is a zero rotation region, which corresponds to the active dislocation movement of slip system (2). In the rightmost part of Figure 6, there is a positive lattice rotation region, which is caused by the active dislocation movement of slip system (3). All these features are comparable to the experimental results as will be shown in Section 4.2.

## 4.2. Experimental results.

**4.2.1. Load displacement relation.** Figure 7a is the loading profile recorded by the data acquisition unit connected to the materials testing system. As can be seen from Figure 7a, the loading and unloading processes were performed by applying a triangle waveform. It is noted that the loading level is normalized by the width of the single crystal such that the unit of the loading is N/mm. The load-displacement relation corresponding to the loading and unloading behavior of the copper single crystal under the wedge indentation is shown in Figure 7b from which two stages of deformation can be seen. The first stage is the elastic-plastic deformation associated with loading. This stage lasts until the load reaches the peak point A as shown in Figure 7b. The total deformation (penetration depth) is about 0.4 mm. The second stage shows elastic unloading and a large hysteresis area under the load displacement curve, as shown in Figure 7b, reveals that the plastic deformation is the dominant mechanism during the indentation process. The second stage finishes once the load drops to point B in Figure 7b. It can be seen that the elastic part of deformation is about 0.03 mm, which can be calculated from the difference in displacement between points A and B on the plot. During the loading process, with the increasing of the loading time, the indentation penetration depth increases almost linearly as shown in Figure 7c. This reveals that the



**Figure 4.** Configuration of the three slip systems.

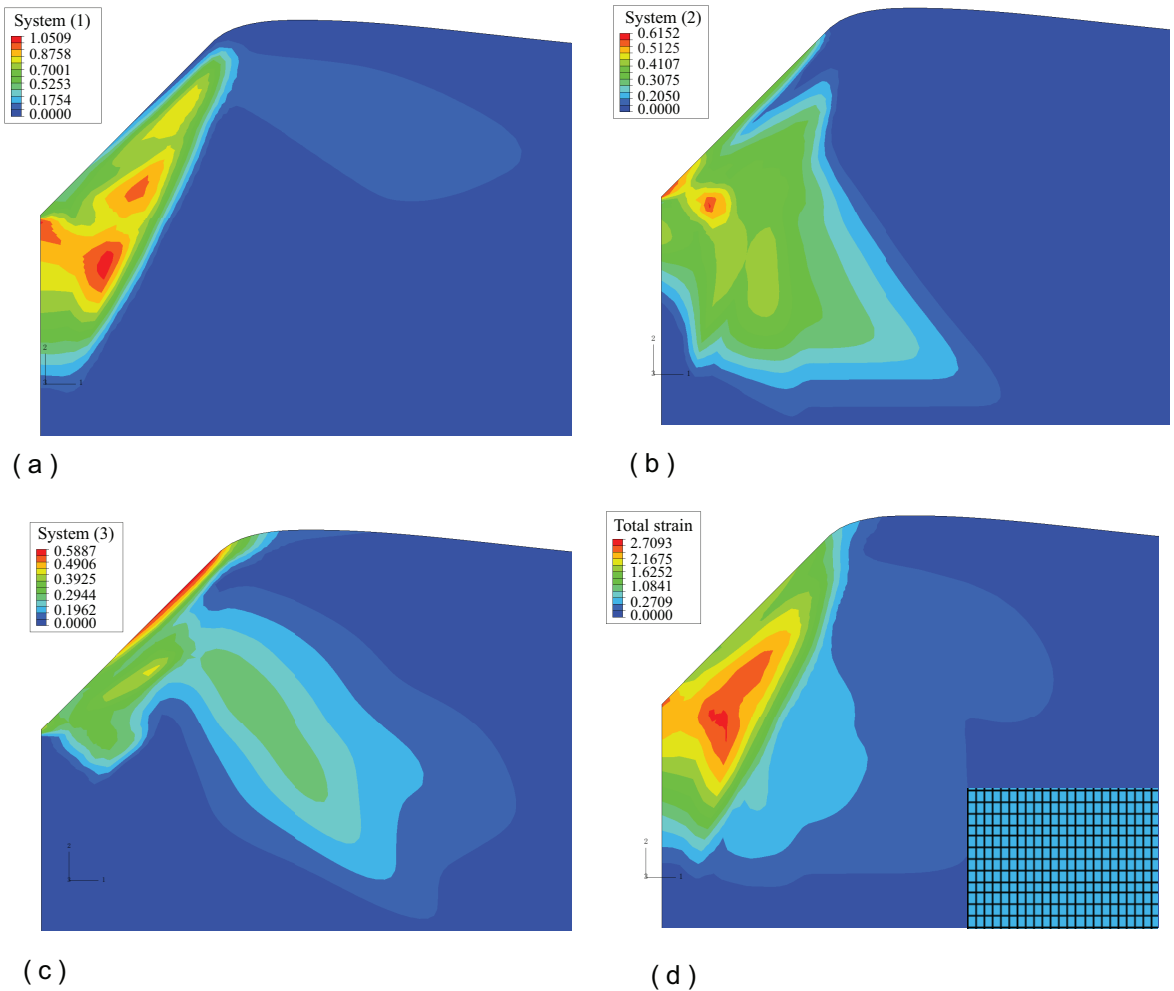


**Figure 5.** Numerical solutions to the shear strains under wedge indentation (deformed state): (a) shear strain of slip system (1),  $\gamma^{(1)}$ , (b) shear strain of slip system (2),  $\gamma^{(2)}$ , (c) shear strain of slip system (3),  $\gamma^{(3)}$ , and (d) the total shear strain,  $\gamma$ . The lower right corner shows the mesh with dimensions  $1.5 \times 1.5 \mu\text{m}$ .

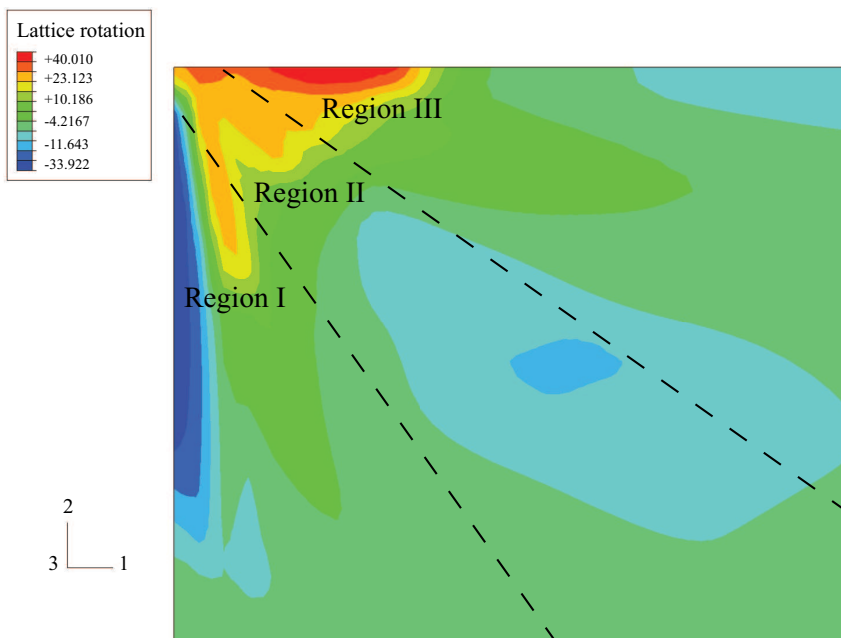


**Figure 6.** Numerical solution to the in-plane crystal lattice rotation showing three distinct regions. The unit of rotation is degree.

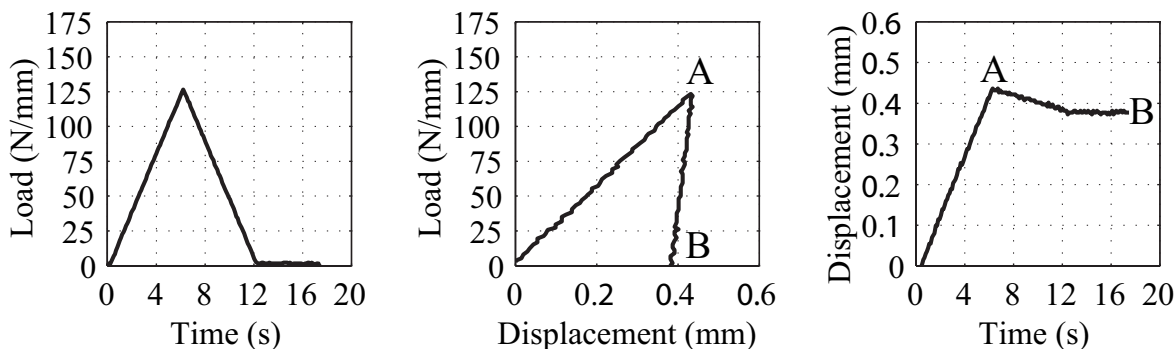


**Figure 7.** Load-displacement response during wedge indentation. Left: the triangle waveform showing force control mode. Middle: load-displacement relation. Right: displacement versus time.

averaged behavior of the copper single crystal is close to ideally plastic in the first deformation stage since the load carrying area increases linearly with the increasing of indenter penetration depth.

**4.2.2. Lattice rotation map of indented copper single crystal.** A schematic of the indented region and the EBSD mapped area for data analysis are illustrated in Figure 8a. In Figure 8b, a contour plot showing the in-plane lattice rotation associated with the wedge indentation is given. It is found from Figure 8b that different regions with distinct lattice rotation features exist underneath the indented region. The change of crystal lattice rotation is in the range from about  $20^\circ$  to  $-20^\circ$ . The highest value is about  $35^\circ$ , and

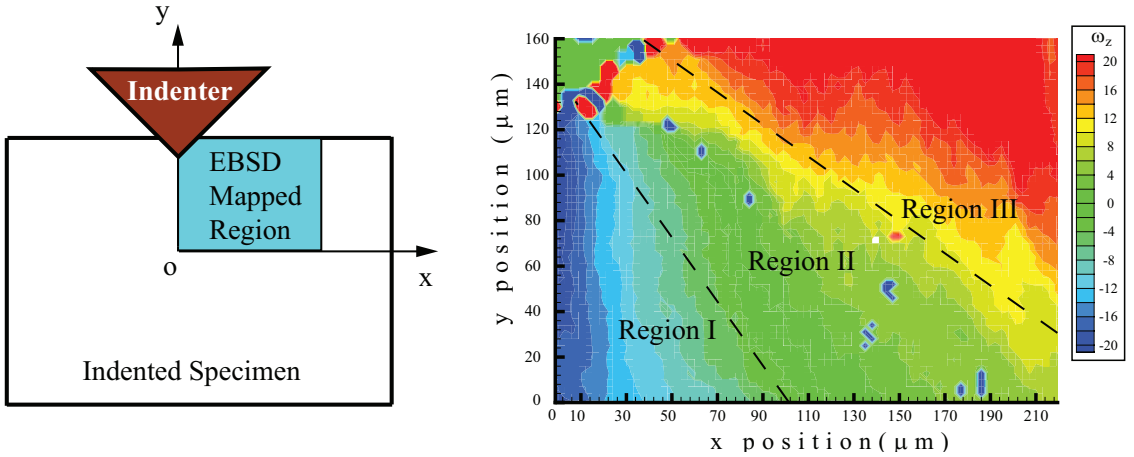


**Figure 8.** EBSD measured in-plane lattice rotation of a copper single crystal under wedge indentation. Left: sketch of the mapped region. Right: lattice rotation contour plot. The unit of in-plane rotation angle,  $\omega_z$ , is the degree.

the lowest value is  $-37^\circ$ . Such scattering values are from the local damage of the specimen. Chemical adsorption in some areas also results in scattering of the measuring results.

It is interesting to examine the evolution of plastic deformation features through the thickness of the indented specimen. Generally, the lattice rotation data taken from a section away from the midplane will show out-of-plane rotation because there is plastic flow along the through thickness direction, that is, the axis of indentation. To demonstrate this, we performed optical examination on the side surface of the indented specimen. Figure 9 is the optical image of the side surface. A sketch of the indenter is also included in the picture to show the relative size of the indented region. Plastic deformation in the forms of shear lines and rings can be observed. Since this surface was not polished, the three slip zones are clearly shown at different levels. The extrusion stages due to the out-of-plane lattice rotation is especially found in Region II of Figure 8b. It is predicted that the magnitude of the out-of-plane lattice rotation is related to the thickness of the specimens. Obviously, systematic experimental studies are needed for generating a series of lattice rotation maps from the locations along the indenter axis, which is one of the important aspects in our future work.

**4.3. Comparison of numerical solutions and experimental results.** As compared with the results shown in Figure 6 (numerical solutions), it can be seen that the in-plane crystal lattice rotation map of Figure 8b can also be divided into three distinct regions in a quadrant. The one with negative lattice rotation is due to the active dislocation motion of slip system (1), as shown in Figure 4. The zero lattice rotation region is corresponding to the active dislocation movement of slip system (2). The positive lattice rotation region is due to the active dislocation movement of slip system (3) as also shown in Figure 4. Thus, the salient features of the in-plane lattice rotation as determined by EBSD experiments are comparable to the results as predicted by the finite element simulations shown in Figure 6. It is noted that there is some difference in lattice rotation quantity between the results shown in Figure 6 and Figure 8b. In the qualitative sense,

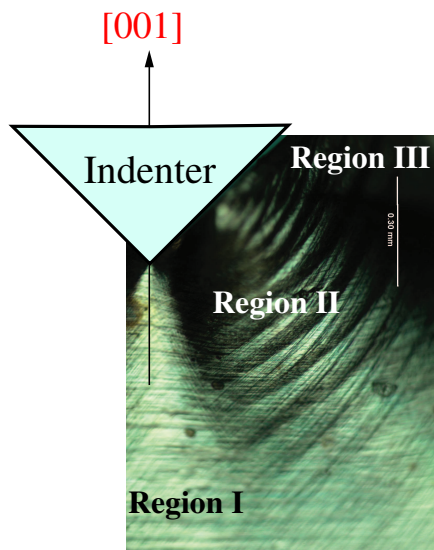


**Figure 9.** Optical micrograph showing plastic deformation in the form of extrusion stages due to the out-of-plane lattice rotation.

it is still reasonable to say that the numerical solutions agree with the experimental results. Therefore, the simulations can be validated by the indentation experiments.

The measured texture component map is also compared with the prediction from the plasticity theory and the finite element simulation results. In **Figure 10**, the  $[110]$  texture component along the  $x$ -axis is shown. The dark color stands for 100% of materials being oriented along the  $\langle 110 \rangle$  crystallographic direction. The brighter and yellow colored areas are those regions with misorientation. The orientation of the materials in these regions shifts away from the  $[110]$  direction. The maximum shift was found to be  $35^\circ$  (this is not marked in **Figure 10** because texture component maps generated by the software have

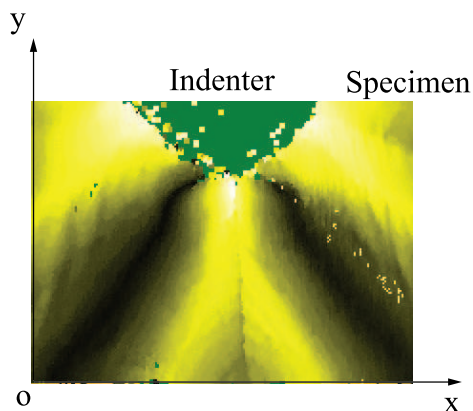


**Figure 10.** Texture component of indented copper single crystal ( $[110]$  texture along  $x$ -direction) showing the plastic spin predicted by the single crystal plasticity theory and the finite element simulation.

no contour legends). Comparing the features shown in Figure 10 with those obtained through numerical simulations (see Figure 6), it is found that a zero-lattice rotation region (Region II) located in the the same area. It must be pointed out that single crystal plasticity theory also predicts the existence of a zero-lattice rotation region associated with the dislocation activities associated with slip system (2), the complex slip system. Regions I and III are separated by this zero-lattice rotation region, as shown in Figure 6, the numerical results.

The numerical simulations as described in this study have a relatively low cost as compared with the experiments. Despite its simplicity, some of the most essential features of wedge indentation, including lattice rotation, can be well captured by the model. We note that in most indentation experiments, especially the sharp indentation tests, a nominally constant plastic strain impression is generated which does not allow the behavior of tested materials to be measured directly. For that matter, construction of equivalent stress fields, strain, and lattice rotation responses of materials with finite element simulations is necessary and could reveal important indentation mechanisms. The importance of numerical simulations becomes more evident through their qualitative agreement with experiment. Further improvements on the simulation method to obtain more accurate results and better quantitative agreements with experiment remain our future work. One of the possible directions is to modify the single crystal plasticity constitutive model. We also expect to simulate different crystals and use different shapes of indenter tip.

It must be pointed out that the preliminary work presented here is based on the special orientation of the crystal, meaning the [001] crystallographic orientation. The results obtained here are useful for dealing with the polycrystal cases, since an arbitrarily selected orientation of a crystal (designated as  $[hkl]$ ) can always be mapped into other orientations by a series of rotation transformations. Thus, a general grain can be treated through transformations such that its orientation matches the [001] case. Accordingly, the modification on the materials subroutine for simulations is needed, and the output variables such as stresses and strains can be obtained by tensorial transformations. For multiple grains, a statistic model may be necessary to accommodate the interactions of different grains and the effect of the grain boundaries. Such a complex case remains to be the topic for future study.

## 5. Conclusions

Based on the experimental studies and finite element simulations of wedge indentation into face-centered cubic (FCC) copper single crystals, the following conclusions are made:

- (1) Finite element simulations of the wedge indentation into the copper crystal have provided stress, shear strain, and in-plane lattice rotation solutions. The results reveal highly heterogeneous plastic deformation behavior of the single crystals under wedge indentation with deep penetration depth.
- (2) The load-displacement relation of the single crystal under wedge indentation shows a plastic deformation dominated behavior. The load increases almost linearly with the indentation penetration depth. Taking into account that the indentation contact area also increases linearly, the elastic ideally plastic behavior of the crystal can be deduced.
- (3) The crystal lattice rotation measurements show three distinct regions in a quadrant, revealing three slip zones. These results show the existence of different single slip sectors in the region within the single crystal underneath the indenter tip as predicted by the single crystal plasticity theory and the finite element simulations.

- (4) The numerical solutions also predict the occurring of dislocation movement along different effective slip systems activated by the wedge indentation. Therefore, the finite element solutions to both the plastic shear strain and lattice rotation are qualitatively validated by the electron backscatter diffraction (EBSD) experimental results. The plastic spin is also verified by the texture component measurement.

**Acknowledgments.** This work was supported in part by University of Toledo Research Awards and Fellowship (URAF) Programs. We appreciate the reviewers for their valuable suggestions on modification of the paper.

## References

- [Asaro 1983] R. J. Asaro, “[Micromechanics of crystals and polycrystals](#)”, *Adv. Appl. Mech.* **23** (1983), 1–115.
- [Beghini et al. 2006] M. Beghini, L. Bertini, and V. Fontanari, “[Evaluation of the stress-strain curve of metallic materials by spherical indentation](#)”, *Int. J. Solids Struct.* **43**:7–8 (2006), 2441–2459.
- [Bhattacharya and Nix 1991] A. K. Bhattacharya and W. D. Nix, “[Finite element analysis of cone indentation](#)”, *Int. J. Solids Struct.* **27**:8 (1991), 1047–1058.
- [Bigot et al. 2005] R. Bigot, V. Favier, and C. Rouff, “[Characterisation of semi-solid material mechanical behaviour by indentation test](#)”, *J. Mater. Process. Technol.* **160**:1 (2005), 43–53.
- [Bolshakov and Pharr 1998] A. Bolshakov and G. M. Pharr, “[Influences of pile-up on the measurement of mechanical properties by load and depth sensing indentation techniques](#)”, *J. Mater. Res.* **13**:4 (1998), 1049–1058.
- [Bouvier and Needleman 2006] S. Bouvier and A. Needleman, “[Effect of the number and orientation of active slip systems on plane strain single crystal indentation](#)”, *Model. Simul. Mater. Sci. Eng.* **14** (2006), 1105–1125.
- [Connolly and McHugh 1999] P. Connolly and P. E. McHugh, “[Fracture modelling of WC-Co hardmetals using crystal plasticity theory and the Gurson model](#)”, *Fatigue Fract. Eng. Mater. Struct.* **22**:1 (1999), 77–86.
- [Fivel et al. 1998] M. C. Fivel, C. F. Robertson, G. R. Canova, and L. Boulanger, “[Three-dimensional modeling of indentation-induced plastic zone at a mesoscale](#)”, *Acta Mater.* **46**:17 (1998), 6183–6194.
- [Follansbee and Sinclair 1984] P. S. Follansbee and G. B. Sinclair, “[Quasi-static normal indentation of an elasto-plastic half-space by a rigid sphere, I: Analysis](#)”, *Int. J. Solids Struct.* **20**:1 (1984), 81–89.
- [Gan et al. 2007] Y. X. Gan, Y. Saito, and X. Chen, “[Cylindrical indentation induced deformation in face-centered cubic metal single crystals](#)”, *J. Mech. Mater. Struct.* **2**:3 (2007), 557–572.
- [Gerberich et al. 2002] W. W. Gerberich, N. I. Tymiak, J. C. Grunlan, M. F. Horstemeyer, and M. I. Baskes, “[Interpretations of indentation size effects](#)”, *J. Appl. Mech. (ASME)* **69**:4 (2002), 433–442.
- [Giannakopoulos et al. 1994] A. E. Giannakopoulos, P.-L. Larson, and R. Vestergaard, “[Analysis of Vickers indentation](#)”, *Int. J. Solids Struct.* **31**:19 (1994), 2679–2708.
- [Habbab et al. 2006] H. Habbab, B. G. Mellor, and S. Syngellakis, “[Post-yield characterisation of metals with significant pile-up through spherical indentations](#)”, *Acta Mater.* **54**:7 (2006), 1965–1973.
- [Havner and Yu 2005] K. S. Havner and P. Yu, “[Kinematic, stress, and hardening analysis in finite double slip](#)”, *Int. J. Plast.* **21**:1 (2005), 83–99.
- [Hill et al. 1989] R. Hill, B. Storakers, and A. B. Zdunek, “[A theoretical study of the Brinell hardness test](#)”, *Proc. R. Soc. Lond. A* **423**:1865 (1989), 301–330.
- [Horstemeyer et al. 2001] M. F. Horstemeyer, M. I. Baskes, and S. J. Plimpton, “[Computational nanoscale plasticity simulations using embedded atom potentials](#)”, *Theor. Appl. Fract. Mech.* **37**:1–3 (2001), 49–98.
- [Hutchinson 1976] J. W. Hutchinson, “[Bounds and self-consistent estimates for creep of polycrystalline materials](#)”, *Proc. R. Soc. Lond. A* **348**:1652 (1976), 101–127.
- [Iost and Bigot 1996] A. Iost and R. Bigot, “[Indentation size effect: reality or artefact?](#)”, *J. Mater. Sci.* **31**:13 (1996), 3573–3577.

- [Kysar 2001] J. W. Kysar, “Continuum simulations of directional dependence of crack growth along a copper/sapphire bicrystal interface, I: Experiments and crystal plasticity background”, *J. Mech. Phys. Solids* **49**:5 (2001), 1099–1128.
- [Kysar et al. 2007] J. W. Kysar, Y. X. Gan, T. L. Morse, X. Chen, and M. E. Jones, “High strain gradient plasticity associated with wedge indentation into face-centered cubic single crystals: geometrically necessary dislocation densities”, *J. Mech. Phys. Solids* **55**:7 (2007), 1554–1573.
- [Laursen and Simo 1992] T. A. Laursen and J. C. Simo, “A study of the mechanics of microindentation using finite elements”, *J. Mater. Res.* **7**:3 (1992), 618–626.
- [Lilleodden et al. 2003] E. T. Lilleodden, J. A. Zimmerman, S. M. Foiles, and W. D. Nix, “Atomistic simulations of elastic deformation and dislocation nucleation during nanoindentation”, *J. Mech. Phys. Solids* **51**:5 (2003), 901–920.
- [Marx and Balke 1997] V. Marx and H. Balke, “A critical investigation of the unloading behavior of sharp indentation”, *Acta Mater.* **45**:9 (1997), 3791–3800.
- [Miller et al. 2004] R. E. Miller, L. E. Shilkrot, and W. A. Curtin, “A coupled atomistics and discrete dislocation plasticity simulation of nanoindentation into single crystal thin films”, *Acta Mater.* **52**:2 (2004), 271–284.
- [Naghdbadi et al. 2005] R. Naghdabadi, M. Yeganeh, and A. R. Saidi, “Application of corotational rates of the logarithmic strain in constitutive modeling of hardening materials at finite deformations”, *Int. J. Plast.* **21**:8 (2005), 1546–1567.
- [Peirce et al. 1983] D. Peirce, R. J. Asaro, and A. Needleman, “Material rate dependence and localized deformation in crystalline solids”, *Acta Metall.* **31**:12 (1983), 1951–1976.
- [Pelletier 2006] H. Pelletier, “Predictive model to estimate the stress-strain curves of bulk metals using nanoindentation”, *Tribol. Int.* **39**:7 (2006), 593–606.
- [Potirniche et al. 2006] G. P. Potirniche, J. L. Hearndon, M. F. Horstemeyer, and X. W. Ling, “Lattice orientation effects on void growth and coalescence in fcc single crystals”, *Int. J. Plast.* **22**:5 (2006), 921–942.
- [Premachandran and Horii 1994] R. Premachandran and H. Horii, “A micromechanics-based constitutive model of polycrystalline ice and FEM analysis for prediction of ice forces”, *Cold Regions Sci. Tech.* **23**:1 (1994), 19–39.
- [Qu et al. 2006] S. Qu, Y. Huang, G. M. Pharr, and K. C. Hwang, “The indentation size effect in the spherical indentation of iridium: a study via the conventional theory of mechanism-based strain gradient plasticity”, *Int. J. Plast.* **22**:7 (2006), 1265–1286.
- [Rashid et al. 1992] M. M. Rashid, G. T. Gray, III, and S. Nemat-Nasser, “Heterogeneous deformations in copper single crystals at high and low strain rates”, *Philos. Mag. A* **65**:3 (1992), 707–735.
- [Savage et al. 2004] P. Savage, B. P. O. Donnell, P. E. McHugh, B. P. Murphy, and D. F. Quinn, “Coronary stent strut size dependent stress-strain response investigated using micromechanical finite element models”, *Ann. Biomed. Eng.* **32**:2 (2004), 202–211.
- [Shu and Barlow 2000] J. Y. Shu and C. Y. Barlow, “Strain gradient effects on microscopic strain field in a metal matrix composite”, *Int. J. Plast.* **16**:5 (2000), 563–591.
- [Sinclair et al. 1985] G. B. Sinclair, P. S. Follansbee, and K. L. Johnson, “Quasi-static normal indentation of an elasto-plastic half-space by a rigid sphere, II: Results”, *Int. J. Solids Struct.* **21**:8 (1985), 865–888.
- [Tadmor et al. 1996] E. B. Tadmor, M. Ortiz, and R. Phillips, “Quasicontinuum analysis of defects in solids”, *Philos. Mag. A* **73**:6 (1996), 1529–1563.
- [Turkmen et al. 2004] H. S. Turkmen, M. P. Miller, P. R. Dawson, and J. C. Moosbrugger, “A slip-based model for strength evolution during cyclic loading”, *J. Eng. Mater. Technol. (ASME)* **126**:4 (2004), 329–338.
- [Vlassak and Nix 1994] J. J. Vlassak and W. D. Nix, “Measuring the elastic properties of anisotropic materials by means of indentation experiments”, *J. Mech. Phys. Solids* **42**:8 (1994), 1223–1245.
- [Wallin and Ristinmaa 2005] M. Wallin and M. Ristinmaa, “Deformation gradient based kinematic hardening model”, *Int. J. Plast.* **21**:10 (2005), 2025–2050.
- [Wang et al. 2004] Y. Wang, D. Raabe, C. Klüber, and F. Roters, “Orientation dependence of nanoindentation pile-up patterns and of nanoindentation microtextures in copper single crystals”, *Acta Mater.* **52**:8 (2004), 2229–2238.
- [Xia et al. 2004] Z. H. Xia, W. A. Curtin, and B. W. Sheldon, “A new method to evaluate the fracture toughness of thin films”, *Acta Mater.* **52**:12 (2004), 3507–3517.

- [Xu and Rowcliffe 2002] Z.-H. Xu and D. Rowcliffe, “Method to determine the plastic properties of bulk materials by nanoindentation”, *Philos. Mag. A* **82**:10 (2002), 1893–1901.
- [Yoshino et al. 2001] M. Yoshino, T. Aoki, N. Chandrasekaran, T. Shirakashi, and R. Komanduri, “Finite element simulation of plane strain plastic-elastic indentation on single-crystal silicon”, *Int. J. Mech. Sci.* **43**:2 (2001), 313–333.
- [Yoshioka 1991] M. Yoshioka, “Numerical analysis of slip behavior in the indented MgO single crystal”, *Int. J. Jpn. Soc. Precis. Eng.* **25** (1991), 175–180.
- [Zaafarani et al. 2008] N. Zaafarani, D. Raabe, F. Roters, and S. Zaeferrer, “On the origin of deformation-induced rotation patterns below nanoindenters”, *Acta Mater.* **56**:1 (2008), 31–42.
- [Zhao et al. 2006] M. Zhao, X. Chen, N. Ogasawara, A. C. Razvan, N. Chiba, D. Lee, and Y. X. Gan, “New sharp indentation method of measuring the elastic-plastic properties of compliant and soft materials using the substrate effect”, *J. Mater. Res.* **21**:12 (2006), 3134–3151.
- [Zhao et al. 2007] M. Zhao, X. Chen, Y. Xiang, J. J. Vlassak, D. Lee, N. Ogasawara, N. Chiba, and Y. X. Gan, “Measuring elastoplastic properties of thin films on an elastic substrate using sharp indentation”, *Acta Mater.* **55**:18 (2007), 6260–6274.
- [Zhu et al. 2004] T. Zhu, J. Li, K. J. Van Vliet, S. Ogata, S. Yip, and S. Suresh, “Predictive modeling of nanoindentation-induced homogeneous dislocation nucleation in copper”, *J. Mech. Phys. Solids* **52**:3 (2004), 691–724.
- [Zimmerman et al. 2001] J. A. Zimmerman, C. L. Kelchner, P. A. Klein, J. C. Hamilton, and S. M. Foiles, “Surface step effects on nanoindentation”, *Phys. Rev. Lett.* **87**:16 (2001), #165507.

Received 5 Feb 2008. Revised 8 May 2008. Accepted 10 Oct 2008.

YONG X. GAN: [yong.gan@utoledo.edu](mailto:yong.gan@utoledo.edu)

Department of Mechanical, Industrial and Manufacturing Engineering, University of Toledo, 2801 West Bancroft Street, Toledo, OH 43606, United States

XI CHEN: Department of Civil Engineering and Engineering Mechanics, Fu Foundation School of Engineering and Applied Science, Columbia University, 500 West 120th Street, New York, NY 10027, United States

MANHONG ZHAO: Department of Civil Engineering and Engineering Mechanics, Fu Foundation School of Engineering and Applied Science, Columbia University, 500 West 120th Street, New York, NY 10027, United States